DOI: 10.1002/anie.201100101

Nanoparticles for MR Imaging

Highly Magnetic Core–Shell Nanoparticles with a Unique Magnetization Mechanism**

Tae-Jong Yoon, Hakho Lee, Huilin Shao, and Ralph Weissleder**

Magnetic nanoparticles (MNPs) with high magnetic moments and very small size are under active development, since such materials have growing uses in biotechnology and medicine.[1] Ferromagnetic metals, rather than their corresponding oxides, have been suggested as an ideal constituent for MNPs for their superior magnetization.[2] Unfortunately, monometallic MNPs typically require protective layers to prevent progressive oxidation. To date, however, most core–shell approaches have yielded sub-optimal magnetization, as the shell was formed either by artificially oxidizing the core[3,4] or by coating it with non-magnetic materials.[5]

Here we present an approach to preparing highly magnetic, monometallic MNPs for biomedical use. The particles consisted of an elemental iron (Fe) core and an artificial ferrite shell (Fe@MFe_2O_4, M = Fe, Mn, Co). The Fe cores were enlarged into a thermally stable ferromagnetic state to increase the overall magnetization. Subsequently, protective ferrite shells were grown onto the cores and metal-doped to further enhance magnetization. The resultant particles displayed a unique magnetic feature, the presence of hysteresis with negligible coercivity. Further analysis revealed a novel magnetization process wherein the shell effectively reduces the coercivity of the ferromagnetic cores by leading the magnetization process at small magnetic fields. The resulting MNPs attain high saturation magnetization but with negligible remanence to prevent inter-particle aggregations. The utility of the particles was demonstrated through the highly sensitive detection of proteins in the picomolar ranges and of single cancer cells. The mechanism and MNP featured here could serve as a new strategy in preparing stable, highly magnetic and yet dispersible nanoparticles from ferromagnetic crystals.

We formed Fe MNPs by thermally decomposing iron complex [$Fe(CO)_5$] in the presence of oleylamine (OY) under air-free conditions (see Supporting Information). As previously reported,[4,6] larger Fe MNPs could be obtained by lowering the molar ratio of Fe and OY ([Fe]:[OY]). The resulting particles, however, had irregular sizes and spontaneously aggregated with decreasing OY concentrations (Figure S1). The optimal value of [Fe]:[OY] for monodispersed particles was approximately 12:1, which limited the particle diameter (d) to <8 nm. To overcome this problem, we explored a new approach for increasing the particle size. Based on the rationale that higher reactivity of the decomposed iron would lead to larger particles,[7] we elevated the reaction temperature. Indeed, it was possible to fine-tune the particle size through temperature control (Figure 1a and Figure S2). Furthermore, by fixing [Fe]:[OY] = 12:1, all Fe MNPs were highly soluble and monodisperse with relative size variations of $<5\%$ (Figure S2).

When exposed to air, Fe MNPs were rapidly oxidized and formed a natural iron oxide shell (Fe@FeO; Figure 1b). This shell had an amorphous structure as confirmed by electron diffraction (Figure 1b, inset) and X-ray diffraction (XRD; Figure 1d). The saturation magnetization (M_s) of the shell, estimated using shell-only particles (Figure S2), was very low (8 emu g^{-1}[Fe]). After adjusting for the shell portion, the M_s of the Fe core was measured at 206 emu g^{-1} [Fe], which is close to that of bulk Fe (210 emu g^{-1} [Fe]). The overall M_s for Fe@FeO MNPs, however, was relatively small (92 emu g^{-1} [Fe]) due to the small portion of Fe core. Moreover, the M_s degraded over time (Figure 1e) as the cores were progressively oxidized (Figure S3).

To prevent the core from oxidation, we next coated the as-synthesized Fe MNPs with protective shells of the ferrite structure. Figure 1c shows an example of Fe MNPs encased in Fe_3O_4 (Fe@Fe_3O_4). After synthesizing Fe MNPs, we added Fe-oleate complexes and annealed the mixture at elevated temperatures to initiate ferrite formation. The crystallinity of the shell, characterized by XRD, gradually improved with increasing annealing temperature; and after aging at 300 °C for 1 h, the diffraction pattern matched that of the spinel ferrite structure (Figure 1d). The ferrite shell was polycrystalline presumably to relieve geometrical strain (Figure S4). The relative variation of the overall particle size, however, was maintained at $<7\%$.

[*] Prof. Dr. T.-J. Yoon,[#] [+] Prof. Dr. H. Lee,[+] H. Shao, Prof. Dr. R. Weissleder
Center for Systems Biology
Massachusetts General Hospital/Harvard Medical School
185 Cambridge Street, Boston, MA 02114 (USA)
Fax: (+1) 617-643-6133
E-mail: hlee@mgh.harvard.edu
rweissleder@mgh.harvard.edu
Prof. Dr. R. Weissleder
Department of Systems Biology, Harvard Medical School
200 Longwood Av., Boston, MA 02115 (USA)

[#] Present address: Department of Applied Bioscience
CHA University, Seoul 135-081 (Republic of Korea)

[+] These authors contributed equally to this work

[**] The authors thank C. Ross (MIT) for her generous support in magnetic measurements; R. Zhang, G. Wojtkiewicz, J. Figueiredo, J. Chen and M. Nahrendorf for their assistance in MRI; N. Sergeyev for synthesizing CLIO; D. Issadore, M. Liong and E. Keliher for helpful discussions; Y. Fisher-Jeffes for reviewing the manuscript. This work was supported by National Institute of Health Grants 2R01-EB004626, U54-CA119349, and TPEN contract (HHSN268201000044C).

Supporting information for this article is available on the WWW under http://dx.doi.org/10.1002/anie.201100101.

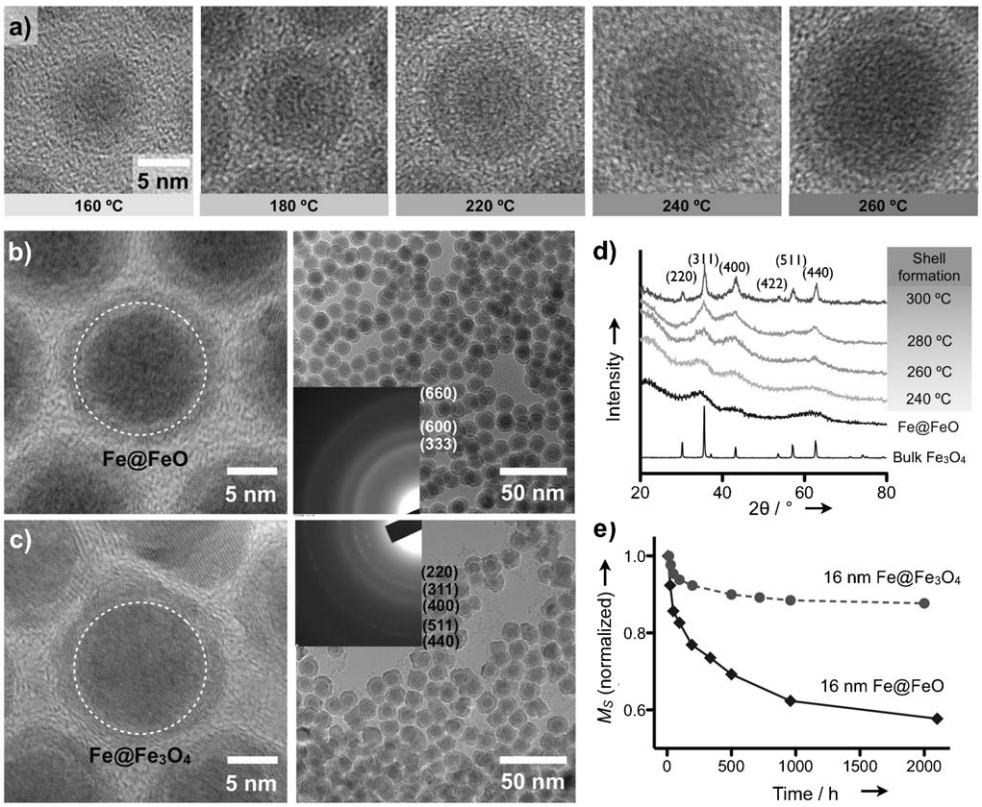

Figure 1. New synthesis of Fe@ferrite MNPs. a) TEM images of a single Fe MNP prepared at different reaction temperatures. The oxide shell was formed while transferring the particles for imaging. b) Fe MNPs were rapidly oxidized to form an oxide shell (Fe@FeO MNPs). The amorphous nature of the shell was confirmed using electron diffraction (ED) patterns (inset). The dotted circle indicates the estimated Fe MNP size prior to oxidation. c) Fe MNPs were encased with crystalline ferrite to provide robust protection from oxidation (Fe@Fe_3O_4). TEM images confirmed that Fe MNPs (dotted circles) were preserved during the coating process. d) The formation of the ferrite shell in (c) was monitored using X-ray diffraction. A typical spinel pattern with sharp peaks was observed at an annealing temperature of 300 °C. Fe@FeO MNPs, in contrast, displayed an amorphous pattern with three main dull peaks. e) Fe@MFe_2O_4 MNPs showed small changes (< 10%) and stable saturation magnetization (M_s) over time, whereas the M_s of Fe@FeO MNPs showed a large (> 40%) and continuous decline.

This approach offers several advantages to improve the magnetic properties of Fe MNPs. First, the ferrite shell protects the Fe core from oxidation. The M_s of the ferrite-coated Fe MNPs were far more stable, reaching a steady value over time (Figure 1e). Second, the ferrite shell could be coated over existing Fe MNPs. Transmission electron microscope (TEM) analysis showed that the size of the Fe core in Fe@Fe_3O_4 was similar to that of the initial diameter of the Fe MNPs (dotted circles in Figure 1c and 1b, respectively). Compared to an alternative method, which oxidizes the surface of Fe MNPs to form a ferrite shell,[3,4] the new approach resulted in larger Fe cores and thereby higher M_s per particle. Third, the shell composition could be changed to tailor the magnetic property of the particles. For example, by co-injecting Mn-oleate or Co-oleate complexes with Fe-oleate ([M]:[Fe] = 1:2; M = Mn, Co), we could obtain Fe@$MnFe_2O_4$ or Fe@$CoFe_2O_4$ MNPs (Figure S4). The $CoFe_2O_4$ shells rendered the particles magnetically hard; whereas the highly magnetic $MnFe_2O_4$ shells made Fe@$MnFe_2O_4$ assume the highest M_s among Fe core MNPs.

The prepared Fe@MFe_2O_4 MNPs (M = Fe, Mn, Co) were made water-soluble by coating their surface with dimercaptosuccinic acid (DMSA). The DMSA-treated MNPs did not elicit acute cytotoxicity when tested at diagnostic concentrations on cancer (HCT116, colon) or on normal (3T3, fibroblast) cells (Figure S5). To render the particles target specific, we conjugated affinity ligands (e.g., biotin, antibody) to the particle surface. The number of antibodies per particle was approximately 10, and the hydrodynamic diameter was ca. 42 nm after conjugation. Note that DMSA coating induced a negative zeta potential on the particles, enhancing the colloidal stability (see Table S1 for details).

Figure 2a shows M_s of Fe@MFe_2O_4 MNPs (d = 16 nm), measured at 2 h after synthesis. For comparative analysis, ferrite MNPs with different compositions were also synthesized (Figure S6). All types of Fe@MFe_2O_4 MNPs had larger M_s than the ferrite ones, with Fe@$MnFe_2O_4$ assuming the largest M_s. The ferrite shells on Fe@MFe_2O_4 were found to have reduced magnetization compared to bulk material, presumably because of the polycrystalline nature of the shell (Table S2). Zero-field-cooled (ZFC) and field-cooled (FC) magnetization (Figure 2b) of Fe@MFe_2O_4 MNPs all displayed peaks at two different temperatures ($T_{B1} > T_{B2}$), denoting the separate onset of superparamagnetism in the Fe core (T_{B1}) and the ferrite shell (T_{B2}).[8] The association of T_{B1} to the Fe core was further confirmed by similar measurements with smaller Fe core MNPs, which showed the shift of T_{B1} toward a lower temperature. Note that T_{B1} was ca. 290 K with 16 nm Fe@MFe_2O_4 which indicated the stable, ferromagnetic nature of the Fe core at room temperature.

The hysteresis loops of Fe@MFe_2O_4 displayed an unusual feature for MNPs: negligible remanence but the presence of hysteresis loss (Figure 2c and Figure S7). For further analysis, the magnetization of Fe@MFe_2O_4 MNPs were calculated using an extended Stoner–Wohlfarth model, which includes the effects of non-zero temperature and cubic magneto-

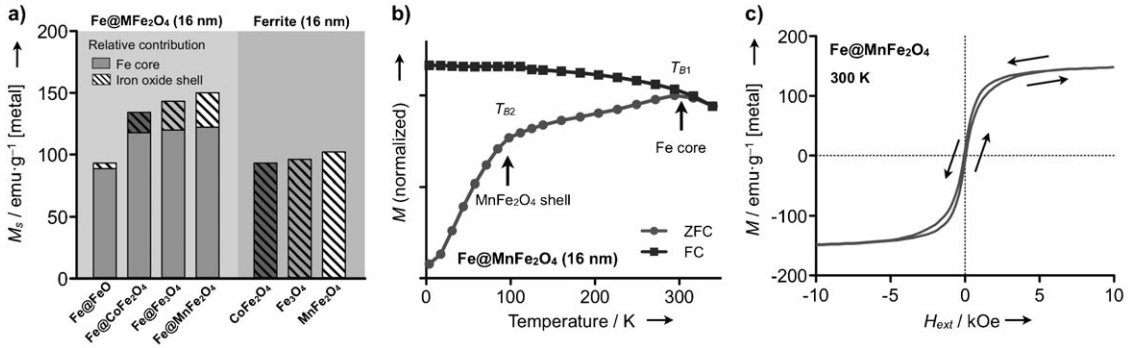

Figure 2. Magnetic properties of Fe@ferrite MNPs. a) All Fe@MFe_2O_4 MNPs ($d = 16$ nm) had higher M_s than similarly sized ferrite MNPs. Among the Fe@MFe_2O_4 MNPs, the overall M_s was within the same order of magnitude as the shell magnetization. b) Temperature-dependent magnetization curves of Fe@$MnFe_2O_4$ MNPs showed distinct peaks at two different temperatures, T_{B1} and T_{B2}, indicating separate onset of superparamagnetism in the core (T_{B1}) and the shell (T_{B2}). c) The field-dependent magnetization (M) of Fe@MFe_2O_4 MNPs at 300 K showed an unusual feature for MNPs: negligible remanent moments but the presence of hysteresis. ZFC, zero-field cooling; FC, field-cooling.

crystalline anisotropy (Figure S8).[9] The simulated magnetization curve showed an excellent agreement with the experimental data (Figure S9), and revealed a novel, cooperative magnetization mechanism. In Fe@MFe_2O_4 MNPs, the shell magnetization (M_{shell}) followed a typical superparamagnetic curve, whereas the core portion (M_{core}) assumed stable single-domain behavior with non-zero coercivity ($H_c =$ 350 Oe; Figure S9). The total magnetization of a particle (M_{tot}), which is the volume-weighted average of M_{core} and M_{shell}, however, displayed considerably less coercivity ($H_c =$ 40 Oe): the superparamagnetic contribution (from the M_{shell}) rapidly saturated to overwhelm the relatively slow magnetization of the core at low magnetic fields. The core contribution (M_{core}) then became dominant at higher magnetic fields to increase the M_{tot}. Note that this unique property rendered the particles both highly magnetic and yet soluble in media.

To evaluate the utility of Fe@MFe_2O_4 MNPs for magnetic resonance(MR)-based sensing, we investigated their transverse relaxivity (r_2), the capacity of MNPs to shorten the transverse relaxation time (T_2) of water. Figure 3a shows the r_2 values of Fe@MFe_2O_4 MNPs along with those of ferrite particles (see Table S3 for details). In general, the r_2 rose with increasing particle size (d), as can be seen among ferrite MNPs. At the fixed size ($d = 16$ nm), the r_2 values were proportional to M_s. Correspondingly, Fe@MFe_2O_4 MNPs had higher r_2 than similarly sized ferrite particles with Fe@$MnFe_2O_4$ assuming the highest value (7×10^{-14} L s^{-1} per particle; 430 s^{-1} mM^{-1} [metal]). When analyzed with an outer-sphere model,[10] the observed r_2 values were highly compatible with theoretical predictions, which validated our approach for enhancing r_2, by increasing both d and M_s. A comparative study of phantoms (Figure 3b) also confirmed the superiority of Fe@$MnFe_2O_4$ as a MR contrast agent; compared to the widely used CLIO (cross-linked iron oxide), Fe@$MnFe_2O_4$ was able to produce the same signal changes at ca. 10 times lower doses. The same trend was observed in the preliminary in vivo imaging (Figure S10).

To demonstrate the biological applications of Fe@MFe_2O_4 MNPs, we used the particles to sense biological markers with the NMR-based diagnostic platform (DMR, diagnostic magnetic resonance).[11] DMR sensing is based on the change of T_2

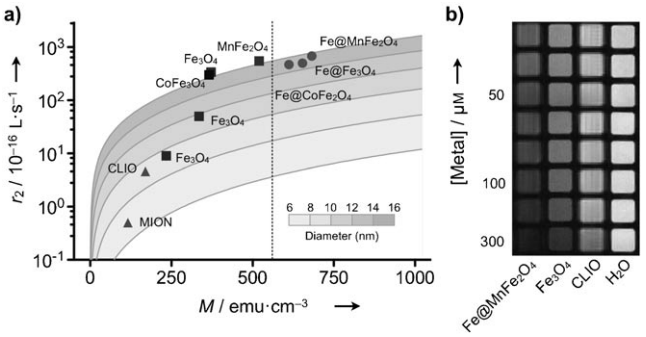

Figure 3. Characterization of transverse relaxivity. a) The transverse relaxivity (r_2) of various MNPs was measured at the fixed Larmor frequency ($f_0 = 20$ MHz; $B_0 = 0.47$ T) and mapped as a function of both the particle size (d) and the magnetization (M) at 0.47 T. Solid lines are calculated using the outer-sphere theory. The r_2 values of ferrite MNPs increased with larger d and M (squares), but were bounded by the intrinsic M of the material (dotted line for bulk $MnFe_2O_4$). Because of their stronger magnetization, Fe@MFe_2O_4 MNPs passed the boundary and attained higher r_2 relaxivities, with Fe@$MnFe_2O_4$ assuming the highest value. b) Phantom images ($f_0 = 300$ MHz; $B_0 = 7$ T) further verified the superiority of Fe@$MnFe_2O_4$ MNPs as imaging agents in MRI. CLIO, cross-linked iron oxide nanoparticle; MION, monocrystalline iron oxide nanoparticle.

(ΔT_2) when detection targets in samples are recognized by MNPs. We first performed molecular detection, using biotin–avidin interaction as a model system. When avidin was added to the solution of biotinylated MNPs, the particles were cross-linked to form nanometer-scale clusters, causing avidin dose-dependent ΔT_2.[11] Among the other types of MNPs, Fe@$MnFe_2O_4$ showed the highest sensitivity by detecting ca. 1.5 pM of avidin (see Supporting Information); the DMR assay thus could be as sensitive as ELISA but with the added advantage of requiring much smaller samples (ca. 1 μL) and shorter assay times (< 30 min).

For cellular detection, we tagged human cancer cells (SkBr3) with MNPs conjugated with HER2/*neu* antibodies. All conjugated MNPs (Fe@$MnFe_2O_4$, Fe_3O_4, CLIO) showed a similar ligand density and a hydrodynamic size (Table S1). Human cells were incubated with MNPs at saturating particle

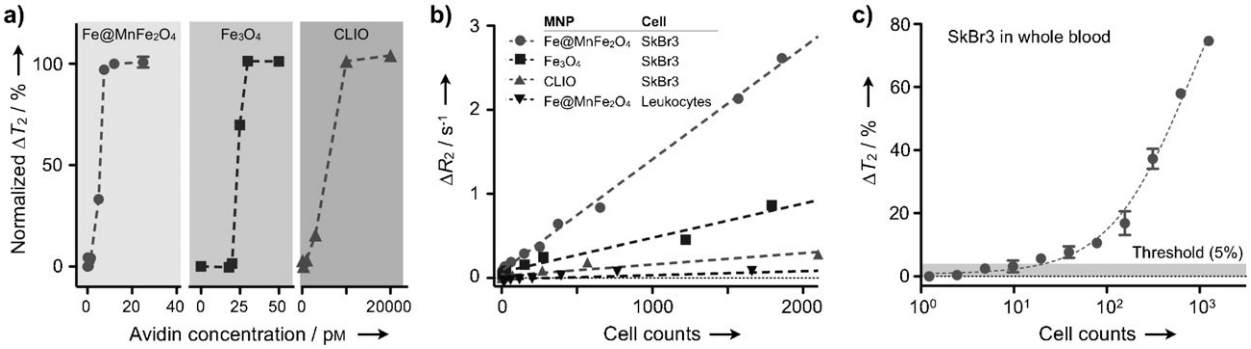

Figure 4. Biological applications of Fe@MFe_2O_4 MNPs. a) The detection of small molecules was demonstrated using biotinylated MNPs. Upon the addition of avidin, biotinylated MNPs aggregated, changing the T_2 of samples. Fe@$MnFe_2O_4$ MNPs showed the best detection threshold (1.5 pM), followed by ferrite (30 pM) and CLIO (2 nM). For each type of MNPs, avidin concentrations yielding $\Delta T_2 \approx 5\%$ were used as detection limits. For clarity, ΔT_2 was normalized against its maximum, and displayed as mean ± s.e.m from triplicate measurements. b) Cancer cells (SkBr3) were targeted with MNPs conjugated with HER2/*neu* antibodies and the relaxation rate ($R_2 = 1/T_2$) was measured in a 1 μL sample volume. Cellular relaxivities (R_2 per cell concentration) followed the same order of particle r_2. Note that host cells (leukocytes) assumed negligible cellular relaxivity. c) Synthetic clinical samples were prepared by spiking SkBr3 cells into human whole blood. After red blood cell lysis, the samples were labeled with HER2/*neu* specific Fe@$MnFe_2O_4$ MNPs. The detection limit was ca. 10 cancer cells even in the presence of abundant host cells. All measurements were performed in triplicate, and the data were displayed as mean ± s.e.m.

concentrations (50 $\mu g\,mL^{-1}$ [metal]) and for a short time (10 min at 37 °C). These conditions were previously shown to minimize nonspecific MNP binding.[12] Following MNP-incubation and removal of unbound MNPs, the T_2 values at different cell concentrations were measured and the cellular relaxivities, defined as the relaxation rate ($R_2 = 1/T_2$) per cell concentration, were obtained (Figure 4b).[12] With the limited numbers of binding sites per cell, cellular relaxivities were found to be in the same order of the particle r_2, with Fe@$MnFe_2O_4$ assuming the highest value ($4 \times 10^{-3}\,\mu L\,s^{-1}$). Host cells (leukocytes) similarly incubated with HER2/*neu*-specific Fe@$MnFe_2O_4$, however, showed ca. 10^3-fold lower cellular relaxivity ($5 \times 10^{-6}\,\mu L\,s^{-1}$), confirming highly selective cell labeling. We next prepared artificial clinical samples by spiking human cancer cells (SkBr3) into human whole blood with erythrocyte lysed, and labeled the samples with HER2/*neu*-specific MNPs. DMR measurements confirmed the superiority of Fe@$MnFe_2O_4$, enabling the detection of ca. 10 cancer cells in the presence of abundant host cells (Figure 4c).

In summary, we have developed a synthetic process for iron core and ferrite shell MNPs, wherein we achieved high magnetization by increasing the core size and modifying the shell composition. Most important, the novel magnetization of the particles provided a new insight into implementing highly magnetic nanoparticles; ferromagnetic cores can be enlarged to enhance the overall magnetic moments, while superparamagnetic shells can retain the core coercivity to prevent inter-particle aggregations. The resulting MNPs assumed high magnetic moments and commensurately high transverse relaxivities, which was utilized in MR-based diagnostics. The particles can also benefit other applications, such as bio-separation (e.g., proteins, cells) and the direct detection of biological targets using magnetometers.

Received: January 6, 2011
Revised: March 3, 2011
Published online: April 14, 2011

Keywords: biosensors · iron · magnetic properties · magnetic resonance imaging · nanoparticles

[1] a) J. Kim, Y. Piao, T. Hyeon, *Chem. Soc. Rev.* **2009**, *38*, 372–390; b) Y. W. Jun, J. W. Seo, J. Cheon, *Acc. Chem. Res.* **2008**, *41*, 179–189.
[2] a) D. Huber, *Small* **2005**, *1*, 482–501; b) Y. Qiang, J. Antony, A. Sharma, J. Nutting, D. Sikes, D. Meyer, *J. Nanopart. Res.* **2006**, *8*, 489–496.
[3] H. Lee, T. J. Yoon, R. Weissleder, *Angew. Chem.* **2009**, *121*, 5767–5770; *Angew. Chem. Int. Ed.* **2009**, *48*, 5657–5660.
[4] S. Peng, C. Wang, J. Xie, S. Sun, *J. Am. Chem. Soc.* **2006**, *128*, 10676–10677.
[5] a) Z. Ban, Y. A. Barnakov, F. Li, V. O. Golub, C. J. O'Connor, *J. Mater. Chem.* **2005**, *15*, 4660–4662; b) J. Cheng, X. Ni, H. Zheng, B. Li, X. Zhang, D. Zhang, *Mater. Res. Bull.* **2006**, *41*, 1424–1429.
[6] H. P. Shao, H. Lee, Y. Q. Huang, I. Y. Ko, C. Kim, *IEEE Trans. Magn.* **2005**, *41*, 3388–3390.
[7] J. Park, K. An, Y. Hwang, J. Park, H. Noh, J. Kim, J. Park, N. Hwang, T. Hyeon, *Nat. Mater.* **2004**, *3*, 891–895.
[8] D. Farrell, S. A. Majetich, J. P. Wilcoxon, *J. Phys. Chem. B* **2003**, *107*, 11022–11030.
[9] I. Joffe, R. Heuberger, *Philos. Mag.* **1974**, *29*, 1051–1059.
[10] A. Roch, R. N. Muller, P. Gillis, *J. Chem. Phys.* **1999**, *110*, 5403–5411.
[11] H. Lee, E. Sun, D. Ham, R. Weissleder, *Nat. Med.* **2008**, *14*, 869–874.
[12] H. Lee, T. J. Yoon, J. Figueiredo, F. Swirski, R. Weissleder, *Proc. Natl. Acad. Sci. USA* **2009**, *106*, 12459–12464.

